X-ray emission from the Wolf-Rayet bubble S 308

J.A. Toalá[1,2,†], M.A. Guerrero[1], Y.-H. Chu[3], R.A. Gruendl[3], S.J. Arthur[2], R.C. Smith[4], and S.L. Snowden[5]

[1] *Instituto de Astrofísica de Andalucía, IAA-CSIC, Glorieta de la Astronomía s/n, 18008 Granada, Spain (CSIC), Spain*

[2] *Centro de Radioastronomía y Astrofísica, Universidad Nacional Autónoma de México, Campus Morelia, Apartado Postal 3-72, 58090, Morelia, Michoacán, Mexico*

[3] *Department of Astronomy, University of Illinois, 1002 West Green Street, Urbana, IL 61801, USA*

[4] *NOAO/CTIO, 950 N. Cherry Avenue, Tucson, AZ 85719*

[5] *NASA Goddard Space Flight Center, Code 662, Greenbelt, MD 20771, USA*

[†] toala@iaa.es

ABSTRACT

The Wolf-Rayet (WR) bubble S 308 around the WR star HD 50896 is one of the only two WR bubbles known to possess X-ray emission. We present *XMM-Newton* observations of three fields of this WR bubble that, in conjunction with an existing observation of its Northwest quadrant (Chu et al. 2003), map most of the nebula. The X-ray emission from S 308 displays a limb-brightened morphology, with a 22′ in size central cavity and a shell thickness of ∼8′. This X-ray shell is confined by the optical shell of ionized material. The spectrum is dominated by the He-like triplets of N VI at ∼0.43 keV and O VII at ∼0.5 keV, and declines towards high energies, with a faint tail up to 1 keV. This spectrum can be described by a two-temperature optically thin plasma emission model (T_1 ∼1.1×10^6 K, T_2 ∼13×10^6 K), with a total X-ray luminosity ∼3×10^{33} erg s^{-1} at the assumed distance of 1.8 kpc. Qualitative comparison of the X-ray morphology of S 308 with the results of numerical simulations of wind-blown WR bubbles suggests a progenitor mass of 40 $M_\odot$ and an age in the WR phase ∼20,000 yrs. The X-ray luminosity predicted by simulations including the effects of heat conduction is in agreement with the observations, however, the simulated X-ray spectrum indicates generally hotter gas than is derived from the observations. We suggest that non-equilibrium ionization (NEI) may provide an explanation for this discrepancy.

Subject headings: ISM: bubbles – ISM: individual (S 308) – stars: individual (HD 50896) – stars: winds,outflows – stars: Wolf-Rayet – X-rays: individual(S 308)

1. Introduction

Wolf-Rayet bubbles are the final result of the evolution of the circumstellar medium (CSM) of massive stars with initial masses $M_i \gtrsim 35\ M_\odot$. These stars exhibit high mass-loss rates throughout their lives, peaking during their post-main-sequence evolution that involves a Red Supergiant (RSG) or Luminous Blue Variable (LBV) stage (e.g., Meynet & Maeder 2003) in which the mass-loss rate can be as high as 10^{-4}–$10^{-3}\ M_\odot$ yr^{-1} (Nugis & Lamers 2000), although the stellar wind velocity is low. The final Wolf-Rayet (WR) stage is characterized by a fast stellar wind, which sweeps up, shocks, and compresses the RSG/LBV material. Thin-shell and Rayleigh-Taylor instabilities lead to the corrugation and eventual fragmentation of the swept-up shell (García-Segura et al. 1996a,b; Freyer et al. 2003, 2006; Toalá & Arthur 2011). Clumpy WR wind-blown bubbles have been detected at optical wavelengths around ∼10 WR stars in our Galaxy (Chu et al. 1983;

Gruendl et al. 2000; Stock & Barlow 2010). Their optical emission is satisfactorily modeled as photoionized dense clumps and shell material (Esteban et al. 1993).

X-ray emission has been detected so far in only two WR bubbles, NGC 6888 and S 308 (Bochkarev 1988; Wrigge et al. 1994, 1998; Wrigge 1999; Chu et al. 2003; Wrigge & Wendker 2002; Wrigge et al. 2005; Zhekov & Park 2011). The most sensitive X-ray observations of a WR bubble are those of the northwest (NW) quadrant of S 308 presented by Chu et al. (2003). Their *XMM-Newton* EPIC-pn X-ray spectrum of S 308 revealed very soft X-ray emission dominated by the N VI He-like triplet at ~0.43 keV and declining sharply toward higher energies. This spectrum was fit with a two-temperature optically thin MEKAL plasma emission model, with a cold main component at $kT_1 = 0.094$ keV (i.e., $T_X \sim 1.1 \times 10^6$ K), and a hot secondary component at $kT_2 \sim 0.7$ keV contributing $\leq$6% of the observed X-ray flux. The comparison of the X-ray and optical Hα and [O III] images of S 308 showed that the X-ray emission is confined by the ionized shell.

In this paper, we present the analysis of three additional *XMM-Newton* observations of S 308, which, together with the observation of its NW quadrant presented by Chu et al. (2003), map most of this WR bubble. The spatial distribution and spectral properties of the X-ray-emitting plasma in S 308 derived from these observations are compared to the predictions of new radiation-hydrodynamic models of WR wind-blown bubbles developed by Toalá & Arthur (2011).

2. *XMM-Newton* Observations

The unrivaled sensitivity of the *XMM-Newton* EPIC cameras to large-scale diffuse emission makes them the preferred choice for the observation of S 308. Chu et al. (2003) presented *XMM-Newton* observations of the brightest NW quadrant of S 308 (Wrigge 1999) but, given that the large angular size of S 308 (~40′ in diameter) exceeds the field of view of the EPIC cameras, a significant fraction of the nebula remained unobserved. To complement these observations, additional *XMM-Newton* observations of three overlapping fields covering the northeast (NE), southwest (SW), and southeast (SE) quadrants of the nebula have been obtained. The previous and new observations result in a substantial coverage of S 308. The pointings, dates and revolutions of the observations, and their exposure times are listed in Table 1. In the following, we will refer to the individual observations by the quadrant of S 308 that is covered, namely the NW, NE, SW, and SE quadrants. All observations were obtained using the Medium Filter and the Extended Full-Frame Mode for EPIC-pn and Full-Frame Mode for EPIC-MOS.

The *XMM-Newton* pipeline products were processed using the *XMM-Newton* Science Analysis Software (SAS) Version 11.0, and the Calibration Access Layer available on 2011-09-13. In order to analyze the diffuse and soft X-ray emission from S 308, the *XMM-Newton* Extended Source Analysis Software (XMM-ESAS) package (Snowden et al. 2008; Kuntz & Snowden 2008) has been used. This procedure applies very restrictive selection criteria for the screening of bad events registered during periods of high background to ensure a reliable removal of the background and instrumental contributions, particularly in the softest energy bands. As a result, the final net exposure times resulting from the use of the XMM-ESAS tasks, as listed in Table 1, are noticeably shorter than the original exposure times. Since we are interested in the best time coverage of the central WR star to assess its possible X-ray variability and given that its X-ray emission level is much brighter than that of the mildly enhanced background, we applied less restrictive criteria in selecting good time intervals for this star. The 10–12 keV energy band is used to assess the charged particle background, and we excised periods of high background with EPIC-pn count rates $\geq$1.5 counts s^{-1} and EPIC-MOS count rates $\geq$0.3 counts s^{-1}.

3. Spatial Distribution of the Diffuse X-ray Emission

3.1. Image processing

Following Snowden & Kuntz' cookbook for analysis procedures for *XMM-Newton* EPIC-MOS observations of extended objects and diffuse background, Version 4.3 (Snowden & Kuntz 2011), the XMM-ESAS tasks and its associated Current Calibration Files (CCF), as obtained from ftp://xmm.esac.esa.int/pub/ccf/constituents/extras/esas_caldb,

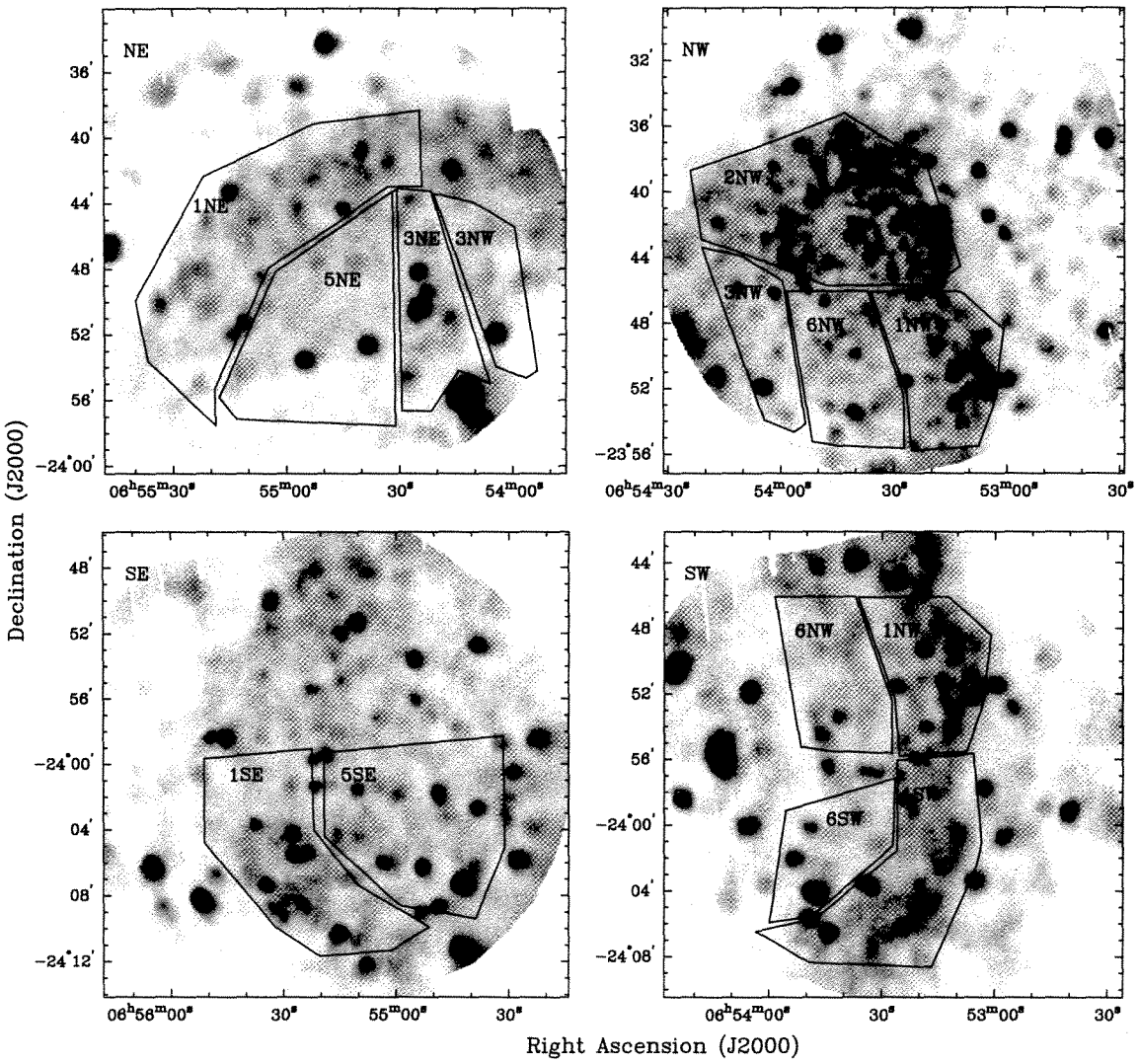

Fig. 1.— *XMM-Newton* EPIC images of the four observations of S 308 in the 0.3–1.15 keV band. The images have been extracted using a pixel size of 2.″0 and adaptively smoothed using a Gaussian kernel between 5″ and 30″. The source regions used for spectral analysis are indicated. Note that the point sources that are present in the images were excised for the spectral analysis.

TABLE 1
XMM-Newton OBSERVATIONS OF S 308

Pointing	R.A. (J2000)	Dec. (J2000)	Obs. ID	Rev.	Observation start UTC	Total exposure time			Net exposure time		
						pn [ks]	MOS1 [ks]	MOS2 [ks]	pn [ks]	MOS1 [ks]	MOS2 [ks]
NW	06:53:30	−23:43:00	0079570201	343	2001-10-23T22:00:09	43.5	47.6	47.5	11.9	19.6	19.9
SW	06:53:24	−23:56:18	0204850401	781	2004-03-15T14:30:41	20.0	23.3	23.4	6.4	9.0	9.2
SE	06:55:16	−24:00:00	0204850501	781	2004-03-14T23:00:41	22.0	25.4	25.4	8.2	12.4	12.7
NE	06:54:47	−23:46:18	0204850601	781	2004-03-15T06:45:41	22.0	25.4	25.4	5.4	8.9	8.4

have been used to remove the contributions from the astrophysical background, soft proton background, and solar wind change-exchange reactions, which have contributions at low energies (<1.5 keV). The resulting exposure-map-corrected, background-subtracted EPIC images of each observed quadrant of S 308 in the 0.3–1.15 keV band are presented in Figure 1. The new observations of the NE, SW, and SE quadrants of S 308 detect diffuse emission, as well as a significant number of point sources superimposed on this diffuse emission. With the single exception of HD 50896 (a.k.a. WR 6), the Wolf-Rayet star progenitor of this bubble registered in the SW and NE observations, all point sources are either background or foreground sources that we have removed prior to our analysis.

3.2. Analysis of the diffuse X-ray emission

In order to analyze the spatial distribution of the diffuse X-ray emission in S 308, the four individual observations have been mosaicked using the XMM-ESAS tasks and all point sources removed using the *Chandra* Interactive Analysis of Observations (CIAO) Version 4.3 *dmfilth* routine, except the one corresponding to WR 6. The final image (Figure 2-*left*), extracted in the 0.3–1.15 keV energy band with a pixel size of 3.″0, has been adaptively smoothed using the ESAS task *adapt-2000* requesting 100 counts of the original image for each smoothed pixel. This image reveals that the diffuse X-ray emission from S 308 has a limb-brightened morphology, with an inner cavity of radius ∼12′. The surface brightness distribution displayed by this image confirms and adds further details to the results of previous X-ray observations (Wrigge 1999; Chu et al. 2003). The X-ray emission from the bubble is brighter towards the northwest blowout and the western rim, and fainter towards the east. The bubble seems to lack detectable X-ray emission towards the central regions around the progenitor WR star.

The limb-brightened spatial distribution of the X-ray emission from S 308 is further illustrated by the surface brightness profiles along the SE–NW and NE–SW directions shown in Figure 3. The emission in the innermost regions, close to the central WR star, falls to levels comparable to those of the background emission shown in the bottom panel of Fig. 3. Besides the SE region, whose surface brightness distribution is best described by a plateau, the X-ray emission along the other directions increases steadily with radial distance, peaking near the shell rim and declining sharply outwards. The thickness of the X-ray-emitting shell is difficult to quantify; along the SW direction, it has a FWHM ∼5′, whereas it has a FWHM ∼8′ along the NE direction. Figure 3 also illustrates that the X-ray-emitting shell is larger along the SE–NW direction (∼44′ in size) than along the NE–SW direction (∼40′ in size).

Finally, the spatial distribution of the diffuse X-ray emission from S 308 is compared to the [O III] emission from the ionized optical shell in Figure 2-*right*. The X-ray emission is interior to the optical emission not only for the NW quadrant but for the entire bubble. This is also illustrated in the color composite picture shown in Figure 4, in which the distribution of the X-ray emission is compared to the optical Hα and [O III] images. This image shows that the diffuse X-ray emission is closely confined by the filamentary emission in the Hα line, whereas the smooth emission in the [O III] line extends beyond both the Hα and X-ray rims.

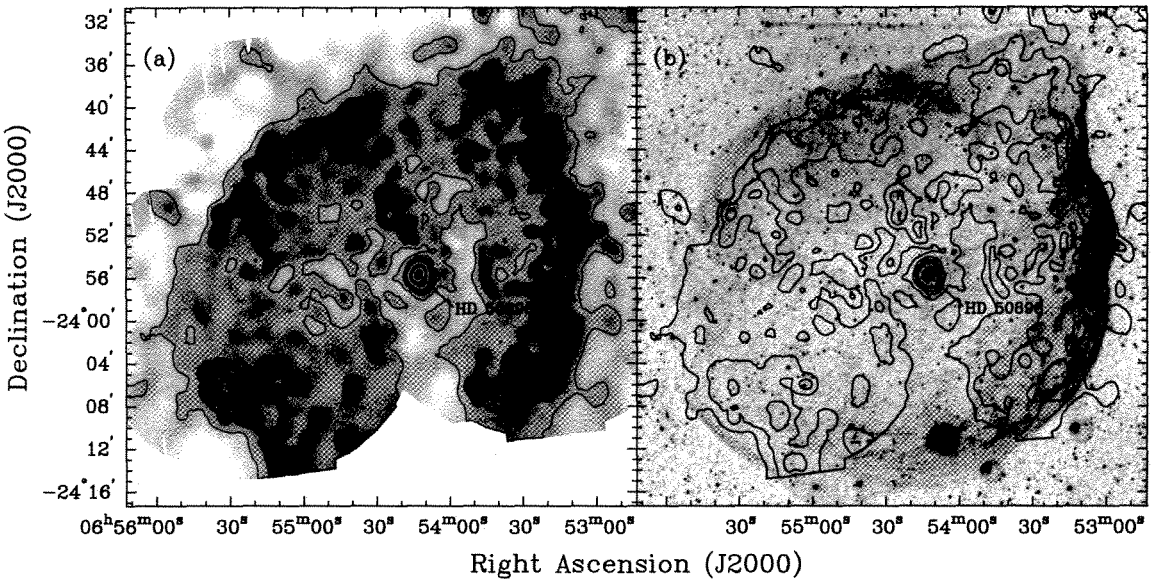

Fig. 2.— *(left)* Adaptively smoothed *XMM-Newton* EPIC Image of S 308 in the 0.3–1.15 keV band. All point sources, except for the central star HD 50896 (WR 6), have been excised. *(right)* Ground-based [O III] image of S 308 obtained with the Michigan Curtis Schmidt telescope at Cerro Tololo Inter-American Observatory (CTIO) with superimposed X-ray emission contours. The position of the central star HD 50896 is indicated in both panels.

4. Physical Properties of the Hot Gas in S 308

The spectral properties of the diffuse X-ray emission from S 308 can be used to investigate the physical conditions and chemical abundances of the hot gas inside this nebula. In order to proceed with this analysis, we have defined several polygonal aperture regions, as shown in Figure 1, which correspond to distinct morphological features of S 308: regions with #1 designations correspond to the rim revealed by the limb-brightened morphology, #2 the NW blowout, #3, #5, and #6 shell interior, and #4 the central star HD 50896. We note that any particular morphological feature may have been registered in more than one quadrant, in which case several spectra can have the same numerical designation (for instance, there are four spectra for the rim of the shell, namely 1NE, 1NW, 1SE, and 1SW).

4.1. Spectra Extraction and Background Subtraction

Perhaps the most challenging problem associated with the analysis of the X-ray spectra of S 308 is a reliable subtraction of the background contribution. The diffuse X-ray emission from S 308 almost fills the field of view of the EPIC-pn and EPIC-MOS cameras, making the selection of suitable background regions difficult because the instrumental spectral response of the cameras close to their edges may not be the same as those for the source apertures.

The background contribution to the diffuse emission from clusters of galaxies that fills the field of view is typically assessed from high signal-to-noise ratio observations of blank fields. In the case of S 308, however, the comparison of spectra extracted from background regions with those extracted from the same detector regions of the most suitable EPIC Blank Sky (Carter & Read 2007) clearly indicates that they have different spectral shapes. The reason for this discrepancy lies in

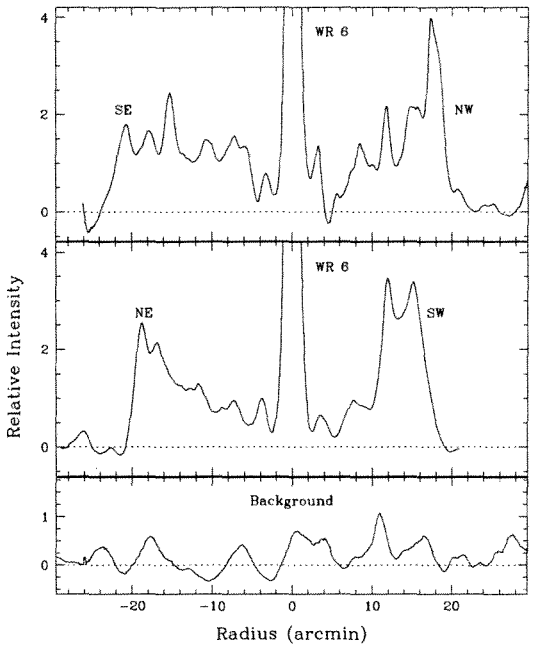

Fig. 3.— S 308 X-ray surface brightness profiles along the SE–NW (PA=135°) and SW–NE (PA=45°) directions extracted from the smoothed *XMM-Newton* EPIC image presented in Figure 2-*left*. For comparison, a surface brightness profile of a representative background region towards the West of S 308 is shown at the same intensity scale.

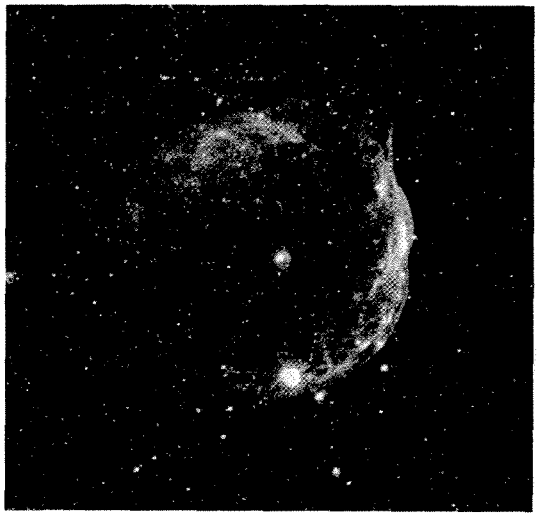

Fig. 4.— Composite color picture of the *XMM-Newton* EPIC image (blue) and CTIO Hα (red) and [O III] (green) images of S 308.

the typical high Galactic latitude of the EPIC Blank Sky observations, implying low hydrogen absorption column densities and Galactic background emission, while S 308 is located in regions close to the Galactic Plane where extinction and background emission are significant. We conclude that EPIC Blank Sky observations, while suitable for the analysis of the diffuse emission of a large variety of extragalactic objects, cannot be used in our analysis of S 308.

Alternatively, the different contributions to the complex background emission in *XMM-Newton* EPIC observations can be modeled, taking into account the contributions from the astrophysical background, solar wind charge-exchange reactions, high-energy (soft protons) particle contributions, and electronic noise. This is the procedure recommended by the *XMM-Newton* Extended Source Analysis Software package (XMM-ESAS) in the release of SAS V11.0, following the background modeling methodology devised by Snowden et al. (2004) and Kuntz & Snowden (2008). Even though the modeling of the different contributions is a complex task, it can be reasonably carried out. Unfortunately, S 308 is projected close to the Galactic Plane in a region of strong soft background emission with spatial variations that cannot be modeled. More importantly, it is not possible to distinguish this background from the soft emission from the S 308 bubble.

Therefore, we have chosen to extract background spectra from the same observations as the source regions (marked in Figure 1) but from areas near the camera edges. The differing spectral responses of the background and central regions to various background components is expected to produce noticeable uncertainties. To assess these uncertainties, we have used the EPIC Blank Sky observations to extract spectra from source and background regions identical in detector units to those used for S 308. Two typical examples of blank sky background-subtracted spectra are presented in Figure 5. While these spectra are expected to be flat, several deviations can be noticed: (1) clear residuals at $\sim$ 7.5 and $\sim$ 8.1 keV, which can be attributed to the defective removal

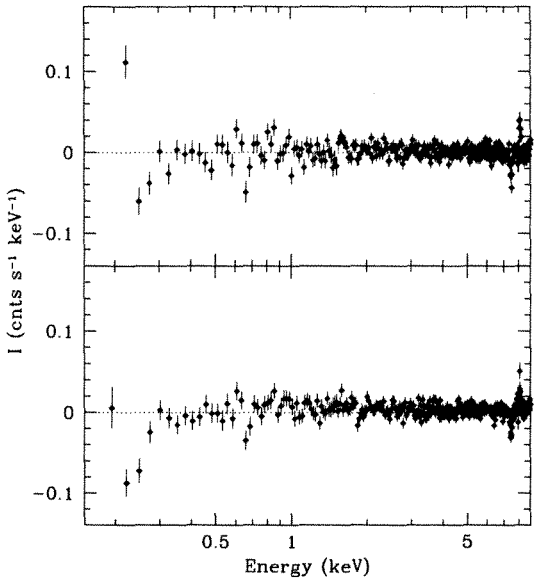

Fig. 5.— Background-subtracted blank sky spectra extracted from source and background regions equal in detector coordinates to the regions 1NW (*top*) and 1SW (*bottom*) of S 308.

of the strong instrumental Cu lines that affect the EPIC-pn spectra (Kuntz & Snowden 2008), (2) a noticeable deviation at ~ 0.65 keV of the O-K line, and (3) most notably, deviations at energies below 0.3 keV, which is indicative of the faulty removal of the electronic noise component of the backround (Carter & Read 2007). Note that the Al-K line at ~ 1.5 keV and the Si-K line at ~ 1.8 keV, which may be expected to be strong in the background EPIC-pn spectra, are correctly removed. Consequently, we have chosen to use the background spectra extracted from the observations of S 308, but restrict our spectral fits to the 0.3–1.3 keV band.

4.2. Spectral properties

The individual background-subtracted EPIC-pn spectra of the diffuse emission of S 308 are presented in Figure 6. This figure also includes spectra of the whole nebula, its rim, and central cavity obtained by combining all spectra, those of regions #1 and #2 (the rim or limb-brightened shell), and those of regions #3, #5, and #6 (the central cavity), respectively. The EPIC-MOS spectra have also been examined and found to be consistent with the EPIC-pn ones although, due to the lower sensitivity of the EPIC-MOS cameras, they have fewer counts. Therefore, our spectral analysis of the diffuse X-ray emission will concentrate on the EPIC-pn spectra.

The spectra shown in Figure 6 are all soft, with a prominent peak at $\gtrsim 0.4$ keV, and a rapid decline in emission towards higher energies. Some spectra (e.g., 1NE, 1NW, 1SW, 5NE, and 5SE) show a secondary peak at $\lesssim 0.6$ keV that can also be hinted in other spectra. There is little emission above ~ 0.7 keV, although some spectra (e.g., 1SE, 1SW, 2NW, 3NE, 5SE, and 6SW) appear to present a hard component between 0.8 and 1.0 keV.

The feature at ~ 0.4 keV can be identified with the 0.43 keV N VI triplet, while the fainter feature at ~ 0.6 keV can be associated with the 0.57 keV O VII triplet. The occurrence of spectral lines is suggestive of optically thin plasma emission, confirming previous X-ray spectral analyses of S 308 (Wrigge 1999; Chu et al. 2003). The predominance of emission from the He-like species of nitrogen and oxygen over their corresponding H-like species implies a low plasma temperature. Furthermore, the relative intensity of the N VI and O VII lines suggests nitrogen enrichment, since the intensity of the O VII lines from a plasma with solar abundances would be brighter than that of the N VI lines.

In accordance with their spectral properties and previous spectral fits of the NW regions of S 308 (Chu et al. 2003), all the X-ray spectra of S 308 have been modeled using a two-temperature APEC optically thin plasma emission model. A low temperature component is used to model the bulk of the X-ray emission, while a high temperature component is used to model the faint emission above 0.7 keV. We have adopted the same chemical abundances as Chu et al. (2003), i.e., C, N, O, Ne, Mg, and Fe to be 0.1, 1.6, 0.13, 0.22, 0.13, and 0.13 times their solar values (Anders & Grevesse 1989), respectively, which correspond to the nebular abundances. The simulated two-temperature APEC model spectra were then absorbed by an interstellar absorption column and convolved with the EPIC-pn response matrices. The resulting spectra were then compared to the observed spectrum in the 0.3–1.3 keV energy range and χ^2 statistics are used to determine the best-fit

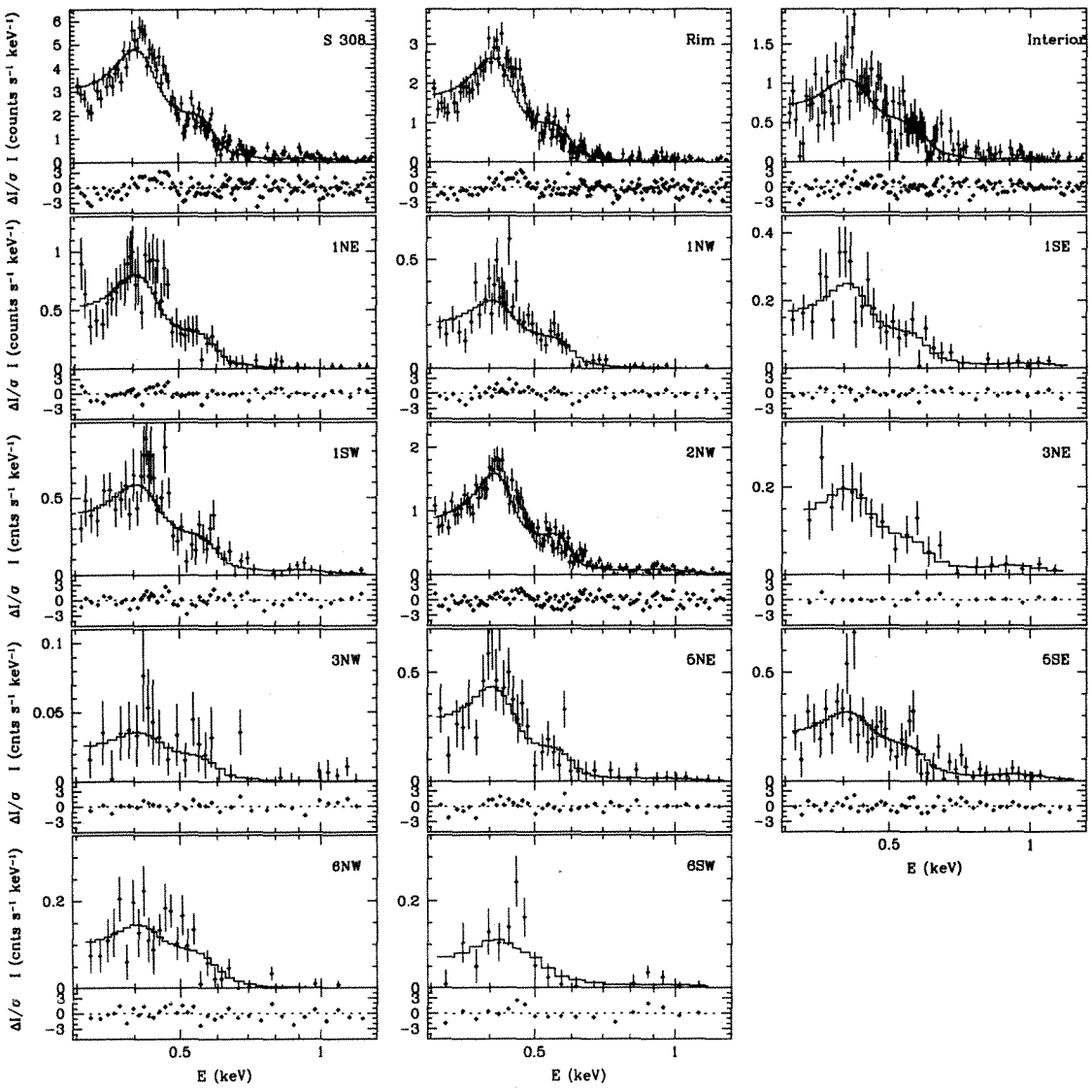

Fig. 6.— Background-subtracted *XMM-Newton* EPIC-pn spectra of S 308 corresponding to the 11 individual source regions shown in Figure 1, as well as to the combined spectra of the entire nebula, its shell or rim (regions #1 and #2) and the interior region of the shell (#3, #5, and #6). Each spectrum is overplotted with its best-fit two-temperature APEC model fit in the energy range 0.3–1.3 keV, assuming fixed abundances, while the lower panels display the residuals of the fit.

TABLE 2
SPECTRAL FITS OF THE DIFFUSE X-RAY EMISSION OF S 308

Region	$N_{\rm H}$ [10^{21}cm^{-2}]	kT_1 [keV]	EM$_1$[a] [cm^{-3}]	f_1[b] [erg cm^{-2}s^{-1}]	kT_2 [keV]	EM$_2$[a] [cm^{-3}]	f_2[b] [erg cm^{-2}s^{-1}]	f_2/f_1	χ^2/DoF
S 308	0.62	0.096±0.002	1.1×10^{57}	2.7×10^{-12}	1.12±0.22	1.7×10^{55}	2.4×10^{-13}	0.090	2.01 (=319.6/159)
Shell	0.62	0.092±0.003	7.1×10^{56}	1.5×10^{-12}	...	...	...	...	1.54 (=233.9/151)
Interior	0.62	0.116±0.011	1.2×10^{56}	5.6×10^{-13}	0.95	6.9×10^{54}	7.5×10^{-14}	0.134	1.35 (=188.2/139)
1NE	0.62	0.094±0.010	2.5×10^{56}	5.1×10^{-13}	0.95	1.6×10^{53}	2.5×10^{-15}	0.005	0.82 (=46.9/57)
1NW	0.62	0.102±0.009	6.8×10^{55}	2.0×10^{-13}	0.95	6.4×10^{50}	1.0×10^{-17}	$< 10^{-3}$	1.13 (=57.9/51)
1SE	0.62	0.094±0.010	2.6×10^{56}	5.1×10^{-13}	0.95	1.6×10^{53}	2.5×10^{-15}	0.005	0.82 (=46.9/57)
1SW	0.62	0.097±0.012	1.5×10^{56}	3.9×10^{-13}	0.95	3.3×10^{54}	5.2×10^{-14}	0.135	1.31 (=69.3/53)
2NW	0.62	0.095±0.003	3.2×10^{56}	7.4×10^{-13}	0.96±0.21	6.2×10^{54}	9.8×10^{-14}	0.130	1.30 (=137.9/106)
3NE	0.62	0.095±0.023	5.0×10^{55}	1.2×10^{-13}	0.95	2.0×10^{54}	3.1×10^{-14}	0.262	0.55 (=9.4/17)
3NW	0.62	0.11±0.04	7.2×10^{54}	2.5×10^{-14}	0.95	8.1×10^{51}	1.2×10^{-16}	0.005	0.91 (=27.4/30)
5NE	0.62	0.090±0.015	1.1×10^{56}	2.1×10^{-13}	0.95	1.3×10^{54}	1.8×10^{-14}	0.083	1.06 (=44.5/42)
5SE	0.62	0.103±0.016	6.3×10^{55}	1.9×10^{-13}	0.95	3.2×10^{54}	5.1×10^{-14}	0.268	1.05 (=54.5/52)
6NW	0.62	0.112±0.015	2.6×10^{55}	1.0×10^{-13}	...	...	...	...	1.42 (=50.0/35)
6SW	0.62	0.12±0.05	1.2×10^{55}	5.7×10^{-14}	0.95	1.4×10^{54}	1.5×10^{-14}	0.270	1.69 (=27.0/16)
W99[c]	3.5	0.129	1.0×10^{56}	...	2.4	4.3×10^{55}	...	...	...
C03[d]	1.1	0.094±0.009	8.2×10^{56}	7.2×10^{-12}	$0.7^{+1.5}_{-0.5}$	5.1×10^{54}	1.1×10^{-13}	0.015	1.02

[a] EM $= \int n_e^2 dV$

[b] Observed (absorbed) fluxes for the two-temperature models components.

[c] Wrigge (1999)

[d] Chu et al. (2003)

models. The foreground absorption ($N_{\rm H}$), plasma temperatures (kT_1, kT_2), and emission measures (EM$_1$, EM$_2$) of the best-fit models are listed in Table 2. The best-fit models are overplotted on the background-subtracted spectra in Figure 6, together with the residuals of the fits. In the following sections we discuss the spectral fits of the emission from the different morphological components of S 308 in more detail.

4.2.1. Properties of the Global X-ray Emission from S 308

The best-fit to the combined spectrum of the whole nebula results in unphysically high values of the hydrogen absorption column density, $N_{\rm H}$, well above the range $[0.2 - 1.05] \times 10^{21}$ cm^{-2} implied by the optical extinction values derived from Balmer decrement of the nebula (Esteban et al. 1992). There appears to be correlated effects of $N_{\rm H}$ and nitrogen abundance on the χ^2 of spectral fits, such that models with high $N_{\rm H}$ and low nitrogen abundance can fit the spectra equally well as models with low $N_{\rm H}$ and high nitrogen abundance. If we adopt the high absorption column density from the best-fit model, the elevated nitrogen abundance reported by Chu et al. (2003) will not be reproduced. As the high absorption column ($N_{\rm H} \gtrsim 3\times10^{21}$ cm^{-2}) is not supported by the optical extinction, in the subsequent spectral fits we will adopt a fixed $N_{\rm H}$ of 6.2×10^{20} cm^{-2} that is consistent with the optical extinction measurements. We note that this choice results in an imperfect modeling of the spectral features in the 0.3–0.5 keV range, as indicated by the S-shaped distribution of residuals in this spectral region in Fig. 6.

The parameters of the best-fit model, listed in the first line of Table 2, show two plasma components at temperatures $\sim1.1\times10^6$ K and $\sim1.3\times10^7$ K with an observed flux ratio, f_2/f_1 ~0.09, corresponding to an intrinsic flux ratio F_2/F_1 ~0.06. The total observed flux is $\sim 3\times10^{-12}$ erg cm^{-2} s^{-1}. The intrinsic luminosity at a distance of 1.8 kpc, after accounting for the fraction of S 308 which is not included in the source apertures considered here, is $\sim3\times10^{33}$ erg s^{-1}. The emission measure of the best-fit to the combined spectrum, along with the spatial distribution of the X-ray-emitting gas in a thick shell with a thickness ~8′, implies an average electron density $n_e \sim 0.1$ cm^{-3}.

4.2.2. *Northwest Blowout (Region #2)*

The northwest blowout of S 308 has the brightest X-ray emission, with a surface brightness $\sim 2.0 \times 10^{-18}$ erg cm^{-2} s^{-1} arcsec^{-2}. Unsurprisingly, the individual spectrum of this region (2NW) has the highest signal-to-noise ratio. The spectral shape is consistent with those of the shell spectra, with a prominent 0.43 keV N VI line, a weaker O VII line, and a clear extension of the spectrum at energies 0.8–1.0 keV. The best fit parameters are rather similar to those of the spectrum of the entire nebula, with a marginally smaller temperature for the hard component. We will adopt this value of the hard component temperature for those regions whose spectra do not have an adequate count number to fit this parameter.

4.2.3. *The Limb-Brightened Shell*

The diffuse X-ray emission from S 308 has a clear limb-brightened morphology surrounding a cavity of diminished X-ray surface brightness. The emission from regions at the rim of this shell (1NE, 1NW, 1SE, and 1SW) is relatively bright, with an averaged surface brightness of the rim $\sim 1.2 \times 10^{-18}$ erg cm^{-2} s^{-1} arcsec^{-2}. All individual spectra of the rim regions show the bright 0.43 keV N VI emission line and indications of the weaker 0.57 keV O VII emission line. The hard component is faint, except for the spectrum of region 1SW. The fit to the combined spectrum confirms the temperature of the soft component, but it is not possible to provide statistical proof of the detection of the hard component. The fits to the individual spectra only provide upper limits for this component, except for region 1SW where it seems relatively bright.

4.2.4. *The Central Cavity*

The level of X-ray emission from the innermost regions of the optical shell of S 308 is lower than that of its edge, with an averaged surface brightness of 5×10^{-19} erg cm^{-2} s^{-1} arcsec^{-2}, i.e., ~ 2.5–4.0 times fainter than the shell and blowout regions. The combined X-ray spectrum of the interior regions shown in Figure 6 indicates a higher contribution of the hard component. This is indeed confirmed by the spectral fit: on average, the hard X-ray component has a flux $\sim 13\%$ that of the soft component. There is a noticeable lack of emission from this component in the region 6NW, but otherwise the average contributions derived from the individual fits are higher than for the spectra of apertures on the shell rim.

4.2.5. *Comparision with Previous X-ray Studies*

Table 2 also lists the best fit parameters of the spectral fits to the diffuse X-ray emission from S 308 obtained by Wrigge (1999) and Chu et al. (2003). It is worthwhile discussing some of the differences with these previous X-ray analyses. The Chu et al. (2003) joint fit of our regions 1NW, 2NW, 3NW and 6NW yields very similar results to the ones shown in Table 2, although their higher foreground absorption ($N_{\rm H} = 1.1 \times 10^{21}$ cm^{-2}) is compensated by our lower temperature for the soft thermal component. For the second thermal component, the derived temperatures from our spectral fits and those of Chu et al. (2003) are consistent with each other, but Wrigge (1999) provides a much higher temperature for this component. This discrepancy highlights the difficulty of fitting the hard component using *ROSAT* PSPC data, as well as the very likely contamination of the *ROSAT* PSPC spectrum of S 308 by unresolved hard point sources embedded in the diffuse emission.

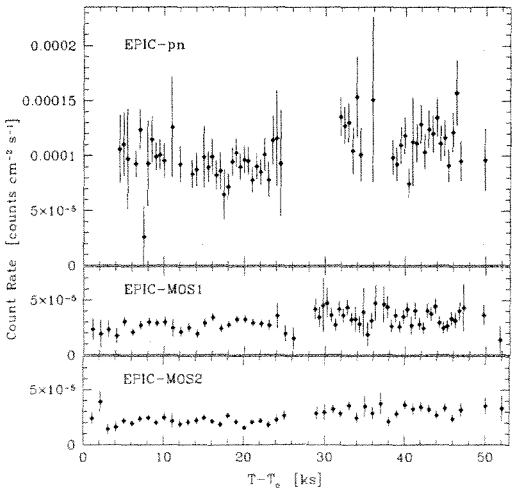

Fig. 7.— EPIC-pn (top), MOS1 (center), and MOS2 (bottom) exposure-map-corrected light curves of WR 6 in the 0.2–9.0 keV energy band. The time is referred to the starting time of the NE observation, 2004-03-15T06:45:41 UTC.

5. The Central Star WR6 (HD 50896)

The central star of S 308 is WR 6 (a.k.a. HD 50896), which has a spectral subtype WN4 (van der Hucht et al. 1988). The star is detected by the *XMM-Newton* EPIC cameras in the NE and SW pointings of the nebula. The EPIC-pn, EPIC-MOS1, and EPIC-MOS2 count rates are 160±4 counts ks^{-1}, 65±2 counts ks^{-1}, and 65±2 counts ks^{-1}, respectively, from the NE observation, and 141±4 counts ks^{-1}, 53±2 counts ks^{-1}, and 52±2 counts ks^{-1}, respectively, from the SW observation. These count rates appear to imply that the X-ray luminosity of WR 6 diminished by 10–20% from the NE to the SW observations, which were only $\sim$ 8 hours apart. We note, however, that these count rates are largely affected by vignetting due to the offset position of WR 6 on the EPIC cameras. Indeed, the light curves shown in Figure 7, after accounting for the effects of vignetting, may imply the opposite, i.e., that the X-ray flux of WR 6 was slightly higher in the second (SW) observation than in the first (NE) observation.

In Figure 8 we present the EPIC background-subtracted spectra for the two different epochs. Following Skinner et al. (2002), we have modeled these spectra with a two-temperature VAPEC model with initial abundances set to those shown in Table 1 of van der Hucht et al. (1986). The fit allowed the foreground absorption column density, temperatures, and abundances of N, Ne, Mg, Si, and Fe to vary (Skinner et al. 2002). The resulting parameters from our best-fit models are displayed in Table 3 for both observations as well as the observed (absorbed) fluxes f, the intrinsic (unabsorbed) fluxes F, and the normalization parameters A[1], compared to those from Skinner et al. (2002). The column density and temperatures of the two components are within 1-σ of each other between the three different models. The observed fluxes are also consistent, although the Skinner et al. (2002) flux seems to be a bit lower, while our fluxes are closer to the ones derived from the October 1995 *ASCA* observations of WR 6 (Skinner et al. 1996). The total observed fluxes and the observed fluxes of the hot thermal component, f_2, listed in Table 3 may indicate a hardening of the X-ray emission from WR 6 in the last SW observation, with an f_2/f_1 ratio of $\sim$ 0.51 for both Skinner et al.'s observation and our NE observation in the energy range of 0.2–10 keV, which increases to 0.57 in the SW observation.

We would like to point out that the column density obtained from our best fits are in good agreement with the values obtained from Skinner et al. (2002), which are higher values compared to the column density used to fit the soft X-ray emission from the nebula. These higher column densities values are commonly observed towards massive stars such as WR stars (Cassinelli et al. 1981; Corcoran et al. 1994; Nazé 2009; Skinner et al. 2010; Gosset et al. 2011).

[1] $A = 1 \times 10^{-14} \int n_e^2 dV / 4\pi d^2$, where d is the distance, n_e is the electron density, and V the volume in cgs units.

6. Discussion

The *XMM-Newton* images and spectra analyzed in the previous sections reveal that the hot plasma in S 308 is spatially distributed in a shell plus the Northwest blowout, with most emission being attributable to a hot plasma at $\sim 1.1 \times 10^6$ K. This low plasma temperature contrasts with the high temperatures ($> 10^7$ K) expected in the shocked stellar wind of WR 6, which has a terminal velocity of 1700 km s^{-1} (Hamann & Koesterke 1998).

Electron thermal conduction has been proposed as a mechanism capable of reducing the temperature of the hot plasma in shocked stellar wind bubbles. The cold shell material from the previous RSG phase is evaporated into the hot bubble, lowering the hot bubble's temperature while raising its density (Spitzer 1962; Cowie & McKee 1977) and hence the cooling rate in the hot gas (e.g., Weaver et al. 1977; Pittard et al. 2001; Steffen et al. 2008). Thermal conduction was applied by Weaver et al. (1977) to stellar wind bubbles to produce a self-similar solution for the density and temperature structure in bubbles. The soft X-ray luminosities predicted by Weaver et al.'s model for the Omega Nebula and the Rosette Nebula, according to the stellar wind parameters of their associated young clusters (M 17 and NGC 2244, respectively), are several orders of magnitude higher than those observed (Townsley et al. 2003; Dunne et al. 2003). Thus, the standard Weaver et al. model for a stellar wind bubble with thermal conduction cannot be taken at face value. Recent

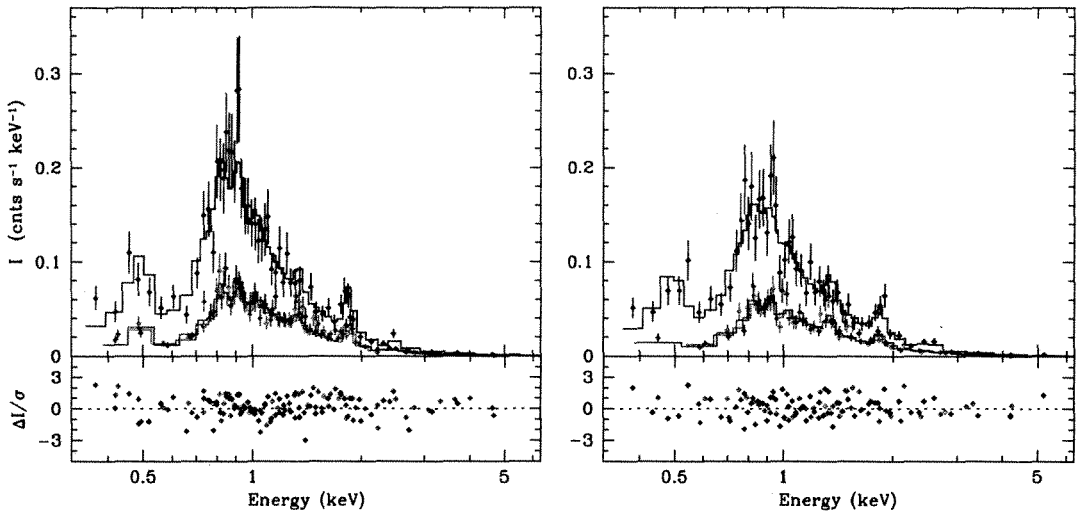

Fig. 8.— Background-subtracted *XMM-Newton* EPIC-pn (black), MOS1 (red), and MOS2 (blue) spectra of WR 6 obtained during the observation of the NE (*left*) and SW (*right*) pointings of S 308.

TABLE 3
SPECTRAL FITS OF HD 50896

Parameter	NE Spectrum	SW Spectrum	Skinner et al. (2002)
N_H [$\times 10^{21}$ cm^{-2}]	$6.4^{+1.0}_{-0.9}$	$5.9^{+1.2}_{-0.9}$	$4.0^{+0.4}_{-0.6}$
kT_1 [keV]	$0.28^{+0.03}_{-0.04}$	0.28	$0.6^{+0.4}_{-0.4}$
A_1 [cm^{-5}]	7.1×10^{-3}	5.9×10^{-3}	3.4×10^{-3}
kT_2 [keV]	$2.5^{+1.5}_{-0.5}$	2.48	$3.5^{+0.7}_{-0.5}$
A_2 [cm^{-5}]	1.8×10^{-4}	2.2×10^{-4}	1.0×10^{-3}
χ^2/DoF	1.10=137.0/124	1.10=113.2/103	1.08=234.5/217
f_1 (0.2–10 keV) [$\times10^{-12}$ erg cm^{-2} s^{-1}]	$1.14^{+0.04}_{-0.24}$	$1.23^{+0.02}_{-0.4}$	0.97
f_1 (2.5–10 keV) [$\times10^{-12}$ erg cm^{-2} s^{-1}]	$0.33^{+0.03}_{-0.07}$	$0.39^{+0.05}_{-0.08}$	0.31
f_2 (0.2–10 keV) [$\times10^{-12}$ erg cm^{-2} s^{-1}]	0.58	0.70	0.49
F_1 (0.2–10 keV) [$\times10^{-12}$ erg cm^{-2} s^{-1}]	19.8	17.6	2.90
F_1 (2.5–10 keV) [$\times10^{-12}$ erg cm^{-2} s^{-1}]	0.35	0.41	0.33
F_2 (0.2–10 keV) [$\times10^{-12}$ erg cm^{-2} s^{-1}]	1.10	1.35	0.78

work by Steffen et al. (2008) in the context of planetary nebulae, which are produced in a very similar manner to WR wind bubbles, has calculated the time-dependent hydrodynamic evolution of planetary nebula wind bubbles including thermal conduction in 1D spherical symmetry. Saturated conduction was taken into account in these calculations by limiting the electron mean free path and it was found that thermal conduction was able to lower the temperature and raise the density at the edge of the hot bubble sufficiently so as to explain the soft X-ray emission and low X-ray luminosities observed in some planetary nebulae (e.g., Chu et al. 2001).

An interesting alternative to thermal conduction for the apparently low temperature of the plasma is non-equilibrium ionization (NEI). Smith & Hughes (2010) calculate the timescales to reach collisional ionization equilibrium (CIE) for ionized plasmas and their results suggest that, for values of the parameters relevant to S 308 (derived electron density of the X-ray emitting plasma of $n_e \sim 0.1$ cm^{-3} and timescale $\sim$ 20,000 yrs, Toalá & Arthur 2011), the CIE assumptions may not hold. We investigate these different possibilities below.

6.1. Thermal conduction efficiency in S 308

We can test the efficiency of thermal conduction in S 308 by analyzing the conduction time of its hot gas. The electron mean free path can be expressed as (Cowie & McKee 1977):

$$\lambda = \frac{10.3}{\ln \Lambda} \left(\frac{T_e}{\mathrm{keV}} \right)^2 \left(\frac{n_e}{\mathrm{cm}^{-3}} \right)^{-1} \mathrm{pc}, \qquad (1)$$

where n_e and T_e are the electron density and temperature in the hot bubble, respectively, and $\ln \Lambda$ is the Coulomb logarithm, which is $\sim$ 35 for the physical conditions typical in S 308 (Spitzer 1962). We estimate the temperature and electron density of the hot bubble in S 308 as $T \sim 4 \times 10^7$ K and $n_e \lesssim 0.01$ cm^{-3}, assuming a stellar wind velocity of 1700 km s^{-1} (Hamann & Koesterke 1998). Therefore, the electron mean free path is $\gtrsim$ 380 pc, which is much larger than the size of S 308. More importantly, in the region where the hot gas abuts the cold shell, the scale length of the temperature gradient, $\ell_{\mathrm{T}} \equiv T_e / |\nabla T_e| \lesssim 1$ pc, is much smaller than the electron mean free path and so the thermal conduction will be saturated (Cowie & McKee 1977).

A conduction timescale can be defined as the time taken for the shock-heated gas to lose its internal energy due to the conductive heat flux through a layer of thickness ℓ_{T} (see, e.g., Sarazin 1988). For saturated thermal conduction, this timescale is of the order

$$t_{\mathrm{sat}} = \frac{3 n_e k T_e \ell_{\mathrm{T}}}{2 q_{\mathrm{sat}}}, \qquad (2)$$

where q_{sat} is the saturated heat flux defined by Cowie & McKee (1977) as

$$q_{\mathrm{sat}} = 0.4 \left(\frac{2kT_e}{\pi m_e} \right)^{1/2} n_e k T_e \ , \qquad (3)$$

and m_e is the electron mass.

For saturated conduction, the conductive effect of the hot electrons should be limited to the sharp edge of the hot bubble, which we identify with the characteristic temperature scale length, ℓ_{T}. The resulting conduction timescale is then

$$t_{\mathrm{sat}} = 360 \left(\frac{\ell_{\mathrm{T}}}{\mathrm{pc}} \right) \left(\frac{T_e}{10^7 \, \mathrm{K}} \right)^{-1/2} \ \mathrm{yrs} \ . \qquad (4)$$

The offset between the X-ray emission in S 308 and the edge of the optical nebula is 2′, which corresponds to 1 pc at a distance of 1.8 kpc. If we adopt a conservative upper limit of 1 pc for ℓ_{T}, using Equation 4 we find that the saturated conduction timescale is < 200 yrs, which is very short compared to the time the central star has spent in the Wolf-Rayet phase ($> 10^4$ yrs). Therefore, we expect thermal conduction to be important at the interface between the cold shell and the hot bubble. On the other hand, we remark that the saturated conduction must be confined to a thin layer at the interface and will not extend throughout the whole bubble (Cowie & McKee 1977).

6.2. Comparison with numerical models

Toalá & Arthur (2011) have performed numerical radiation-hydrodynamic simulations to study wind-wind interactions in the interstellar and circumstellar media (ISM & CSM) around massive stars. In their paper they study the imprint that different stellar evolution models leave in the CSM, and their results are relevant to S 308. The

spectral parameters of WR 6 (a.k.a. HD 50896), the central star of S 308, are consistent with several different publicly available stellar evolution models from the literature (Hamann et al. 2006), for example, the 40 $M_{\odot}$ initial stellar mass models of Meynet & Maeder (2003) (both with and without stellar rotation[2]), and the 45 $M_{\odot}$ initial stellar mass models of STARS (Eggleton 1971; Pols et al. 1995; Eldridge & Tout 2004). The stellar wind parameters derived from these stellar evolution models are not tailored to any particular object, but during the WR stage are reasonably close to the values derived from observations of the central WR star of S 308. The main determining factors in the structure of the wind-blown bubble during the WR stage are found to be the duration of the RSG stage and the velocity of the slow wind (Toalá & Arthur 2011). For a short duration RSG stage with a slow stellar wind, such as results from the STARS stellar evolution models, most of the material expelled during the RSG stage (some 15 $M_{\odot}$) will be within 2 pc of the central star at the onset of the WR stage. On the other hand, the Meynet & Maeder (2003) models have more extended RSG lifetimes and the bulk of the RSG material forms a shell of 6–8 parsecs from the star before the WR stage begins. While the results of the radiation-hydrodynamic simulations using the STARS stellar wind parameters fail to reproduce the morphological features and soft X-ray luminosities of S 308, the results obtained using the evolution models of Meynet & Maeder (2003) are more promising.

Figure 9 shows the density and temperature distributions from a simulation including thermal conduction at a time 1.87×10^4 yrs after the onset of the WR stage for the Meynet & Maeder (2003) stellar model of a 40 $M_{\odot}$ star with rotation. At this time, the dense RSG material, which is swept up by the fast WR wind, has formed a shell with outer radius ($\sim$ 9 pc) and shell thickness ($\sim$ 1 pc) similar to those of S 308. The corresponding soft X-ray luminosity in the 0.3–1.3 keV energy band from this simulation is $\sim 4.3 \times 10^{33}$ erg s^{-1} for the same abundances used in the spectral fit model (see § 4). This luminosity is very close to that determined from the observation, $\sim 3 \times 10^{33}$ erg s^{-1}. Calculations were performed both with

[2]The initial rotation velocity at the equator is 300 km s^{-1}.

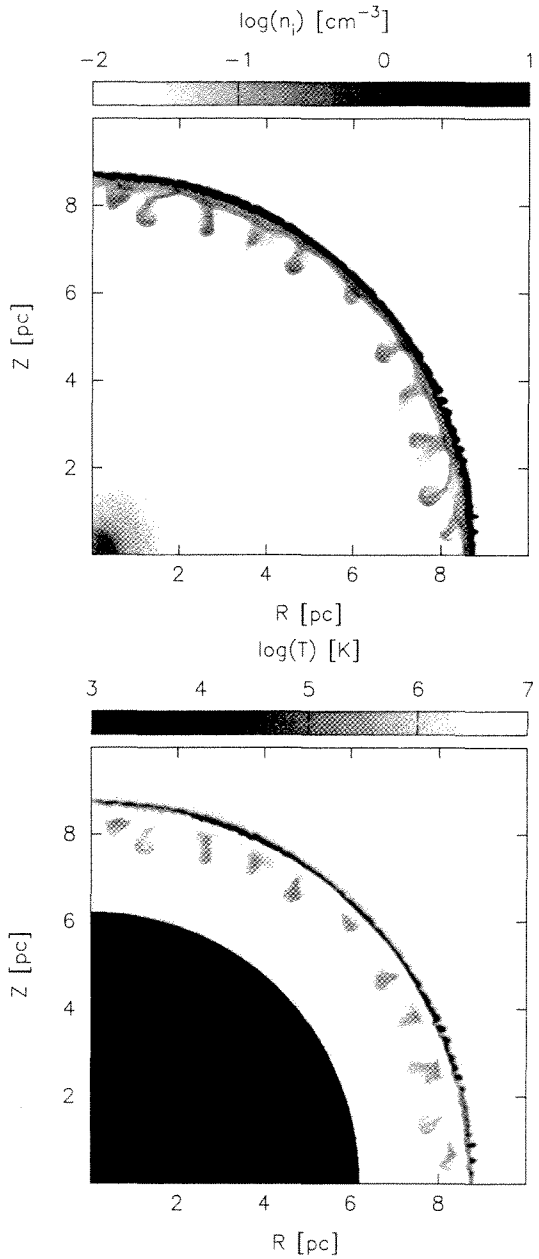

Fig. 9.— Radiation-hydrodynamic numerical simulation of a WR wind-blown bubble for a 40 $M_{\odot}$ stellar model (see text) at a time 1.87×10^4 yrs after the onset of the WR stage. The top panel shows the ionized number density, whereas the bottom panel shows the plasma temperature. The star is located at $(r, z) = (0, 0)$ and the figure shows the computational plane of a 2D cylindrically symmetric calculation. The temperature in the free-flowing wind has been set to 10^4 K.

and without thermal conduction to evaluate the importance of this physical process. While there is little difference between the appearance of the circumstellar structures, the calculated soft X-ray luminosity is lower by an order of magnitude if thermal conduction is not included in this particular model.

In Figure 10 we compare the observed spectrum from the whole nebula with the synthetic spectrum of the X-ray emission corresponding to the numerical simulation presented in Figure 9 using the same abundances and absorbing column density, where we assumed CIE conditions for the calculation of the spectrum. As was discussed in the previous sections, the observed spectrum peaks at the He-like triplet of N VI at 0.43 keV, whereas the synthetic spectrum presents an emission peak at ~ 0.5 keV, which corresponds to the N VII Kα transition, a secondary emission peak at 0.9 keV due to the He-like triplet of Ne IX, and a small emission peak which corresponds to the emission of Fe XVII at 0.75 keV. The N VI/N VII line ratio and the presence of Fe XVII and Ne IX lines in our synthetic spectrum are the result of the emission from plasma at a wide range of temperatures, between 10^6 K and 5×10^6 K, corresponding to shocked RSG material, with a secondary contribution to the spectrum from a plasma at temperatures $\sim 2 \times 10^7$ K, corresponding to shocked stellar wind material. These plasma temperatures are substantially higher than the temperature derived from observations.

6.3. Non-equilibrium ionization

It is generally assumed that CIE holds in the hot, shocked plasma of stellar wind bubbles, i.e., that the ionization fractions of the different species are determined solely by the plasma temperature. In Wolf-Rayet wind bubbles the detected X-rays could be produced by the hot, shocked stellar wind. However, we expect this gas to have temperatures too high ($T > 10^7$ K) and densities too low ($n < 10^{-2}$ cm^{-3}) to match the observations. Alternatively, the X-rays could be emitted by swept-up red supergiant material, which is shocked by the outer shock of the two-shock wind pattern produced when the fast WR wind starts. The red supergiant shell has initial temperatures $\sim 10^4$ K, but once it is swept up by the WR wind its temperature is suddenly raised to $T > 10^6$ K (see Fig. 9).

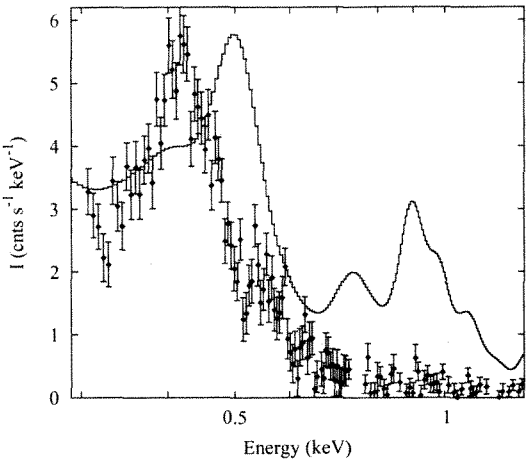

Fig. 10.— Synthetic spectrum of diffuse X-ray emission (solid line) for the WR bubble model presented in Figure 9 compared to the observed spectrum of the whole nebula (diamonds).

Wolf-Rayet wind bubbles have short lifetimes, a few times 10^4 yrs, and this means that the ionization timescales, $n_e t$, of the swept-up red supergiant material may be too long for collisional ionization equilibrium to be attained. As a result, low ionization stages could still be present in important amounts in the hot, shocked RSG material, even though in CIE at the same post-shock temperature the ionization fractions of these species would be negligible.

As an illustration, we consider the non-equilibrium ionization of a plasma initially at 3×10^4 K, which is suddenly shocked by a fast stellar wind. The expected ionization fractions of N VI and N VII, the dominant species in the X-ray spectrum of S 308, are shown in Figure 11 for gas densities $n = 0.1$, 0.2, 0.5, and 1.0 cm^{-3} and timescales up to 50,000 yrs. In this figure, we also show the equilibrium fractions for gas at electron temperature $T_{\rm high} = 3.6 \times 10^6$ K (upper horizontal line), representative of the X-ray-emitting gas found in the numerical simulation shown in Figure 9, and at electron temperature $T_{\rm low} = 1.1 \times 10^6$ K (lower horizontal line) corresponding to that derived from observations of S 308. The spectrum obtained from a plasma out of ionization equilibrium will be markedly different to that obtained under the assumption of CIE, and will depend

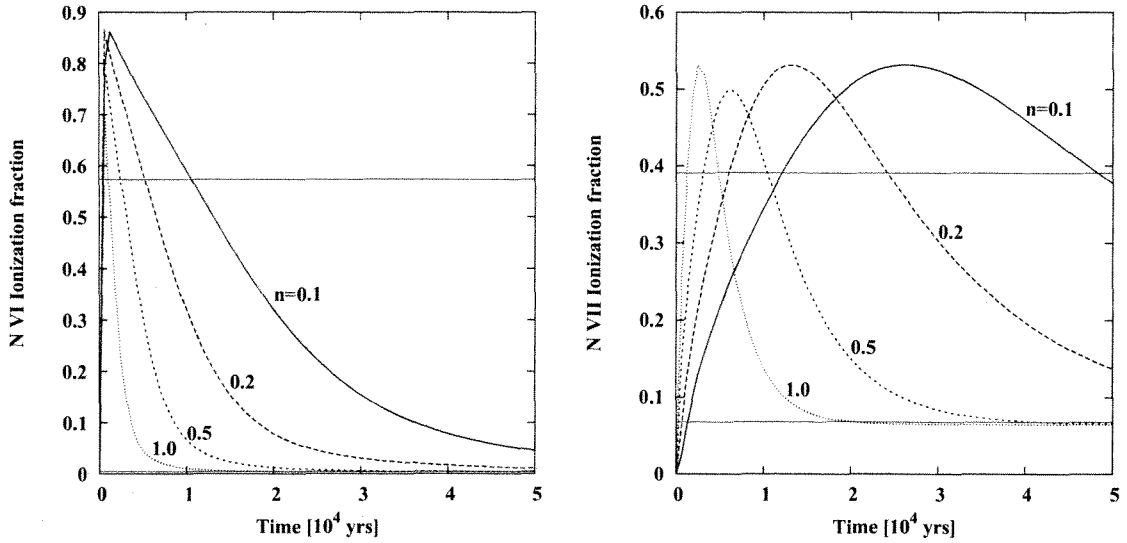

Fig. 11.— Time evolution of the ionic fractions of N VI (*left*) and N VII (*right*) for a plasma under the assumption of non-equilibrium ionization with electron densities 0.1, 0.2, 0.5, and 1.0 cm^{-3}. The lower and upper thin horizontal lines in each figure represent the collisional ionization equilibrium fractions, y_{CIE}, at electron temperatures $T_{\mathrm{high}} = 3.6 \times 10^6$ K and $T_{\mathrm{low}} = 1.1 \times 10^6$ K, respectively, of the corresponding ion.

on the ionization timescale. Low ionization states can persist even though the electron temperature is high, and the resultant spectrum would appear to be much softer than expected. Note that gas with higher densities achieves equilibrium much more rapidly.

Figure 11 shows that, for a gas with electron density $n_e = 0.1$ cm^{-3} (similar to that derived from the observations), at a time 20,000 yrs after the onset of the WR wind (as suggested by the numerical model of § 6.2), the fractions of N VI and N VII for gas in non-equilibrium ionization would be 0.35 and 0.57, respectively. For gas in collisional ionization equilibrium at the postshock temperature of $T_{\mathrm{high}} = 3.6 \times 10^6$ K, the respective fractions would be <0.01 and 0.068. On the other hand, collisional ionization equilibrium at a postshock temperature of $T_{\mathrm{low}} = 1.1 \times 10^6$ K yields a N VI fraction of 0.74 and a N VII fraction of 0.25. The non-equilibrium ion fractions of N VI and N VII are thus closer to those expected for a much lower temperature gas if CIE is assumed and the spectrum will be correspondingly softer.

7. Summary and conclusions

We present *XMM-Newton* observations of three fields of the WR bubble S 308 which, in conjunction with the observation of its NW quadrant presented by Chu et al. (2003), map most of the nebula except for its southernmost section. We have used these observations to study the spatial distribution of the X-ray-emitting material within this bubble, to derive global values for its physical conditions (T_e, n_e), and to search for their spatial variations among different morphological components of the nebula.

The X-ray emission from S 308 is found to have a limb-brightened morphology, with a shell thickness 5′–8′, with the shell thicker at the northwest blowout regions. The X-ray-emitting shell is notably larger along the SE-NW direction than along the SW-NE direction, and it is always confined by the optical shell of ionized RSG material. The X-ray surface brightness emission decreases notably from the blowout region and the western rim shell to the shell interior, where the X-ray emission falls to background levels. The western quadrants are also brighter than the eastern quadrants.

The X-ray emission from S 308 is dominated by the emission from the He-like triplet of N VI at 0.43 keV, shows fainter emission of the O VII 0.5 keV triplet, and declines towards high energies, with a faint tail up to 1 keV. This spectrum can be described by a two-temperature optically thin plasma emission model with temperatures $\sim 1.1 \times 10^6$ K and $\sim 1.3 \times 10^7$ K, with the latter component notably fainter than the former by at least a factor ~ 6. There is an appreciable difference between the relative contributions of the hot component to the X-ray-emitting gas between the rim and the nebula interior, which presents a higher contribution from the hard component. The total X-ray luminosity at a distance of 1.8 kpc is estimated to be $\sim 3 \times 10^{33}$ erg s^{-1} .

The *XMM-Newton* observations of S 308 are compared with the predictions of radiation-hydrodynamic simulations of WR bubbles from models with stellar parameters similar to those of its central star. Models including stellar rotation for a 40 $M_\odot$ progenitor and the inclusion of heat conduction in the calculations provide excellent agreement with the observed morphology and soft X-ray luminosity for a bubble age ~20,000 yrs, but the temperature of the X-ray emitting gas is higher than that derived from the observations. If CIE is assumed, the simulations predict spectra showing higher ionization states than the observations. If the X-ray-emitting plasma were in NEI, then the young age of the bubble and the low densities in the X-ray emitting gas would allow lower ionization states to persist and the synthetic spectrum would more closely resemble the observed one.

The physical conditions, abundances and amount of intervening material derived from spectral fits of the X-ray emission from the central WR star, WR 6, are roughly consistent with previous results. The light curve of the X-ray emission shows tantalizing evidence of variability in time-scales of hours that may also result in variations of the emission hardness.

REFERENCES

Anders, E., & Grevesse, N. 1989, Geochim. Cosmochim. Acta, 53, 197

Arnal, E. M., & Cappa, C. E. 1996, MNRAS, 279, 788

Arthur, S. J. 2007a, Diffuse Matter from Star Forming Regions to Active Galaxies, 183

Balucinska-Church, M., & McCammon, D. 1992, ApJ, 400, 699

Bochkarev, N. G. 1988, Nature, 332, 518

Carter, J. A., & Read, A. M. 2007, A&A, 464, 1155

Cassinelli, J. P., Waldron, W. L., Sanders, W. T., et al. 1981, ApJ, 250, 677

Chu, Y.-H. 2008, IAU Symposium, 250, 341

Chu, Y.-H., Guerrero, M. A., Gruendl, R. A., Williams, R. M., & Kaler, J. B. 2001, ApJ, 553, L69

Chu, Y.-H., Guerrero, M. A., Gruendl, R. A., García-Segura, G., & Wendker, H. J. 2003, ApJ, 599, 1189

Chu, Y.-H., Treffers, R. R., & Kwitter, K. B. 1983, ApJS, 53, 937

Corcoran, M. F., Waldron, W. L., Macfarlane, J. J., et al. 1994, ApJ, 436, L95

Cowie, L. L., & McKee, C. F. 1977, ApJ, 211, 135

Dunne, B. C., Chu, Y.-H., Chen, C.-H. R., Lowry, J. D., Townsley, L., Gruendl, R. A., Guerrero, M. A., & Rosado, M. 2003, ApJ, 590, 306

Eggleton, P. P. 1971, MNRAS, 151, 351

Eldridge, J. J., & Tout, C. A. 2004, MNRAS, 353, 87

Esteban, C., Vílchez, J. M., Smith, L. J., & Clegg, R. E. S. 1992, A&A, 259, 629

Esteban, C., Smith, L. J., Vilchez, J. M., & Clegg, R. E. S. 1993, A&A, 272, 299

Freyer, T., Hensler, G., & Yorke, H. W. 2003, ApJ, 594, 888

Freyer, T., Hensler, G., & Yorke, H. W. 2006, ApJ, 638, 262

García-Segura, G., Mac Low, M.-M., & Langer, N. 1996a, A&A, 305, 229

García-Segura, G., Langer, N., & Mac Low, M.-M. 1996b, A&A, 316, 133

Gosset, E., De Becker, M., Nazé, Y., et al. 2011, A&A, 527, A66

Gruendl, R. A., Chu, Y.-H., Dunne, B. C., & Points, S. D. 2000, AJ, 120, 2670

Hamann, W.-R., Gräfener, G., & Liermann, A. 2006, A&A, 457, 1015

Hamann, W.-R., & Koesterke, L. 1998, A&A, 333, 251

Kuntz, K. D., & Snowden, S. L. 2008, A&A, 478, 575

Meynet, G., & Maeder, A. 2003, A&A, 404, 975

Nazé, Y. 2009, A&A, 506, 1055

Nugis, T., & Lamers, H. J. G. L. M. 2000, A&A, 360, 227

Pittard, J. M., Dyson, J. E., & Hartquist, T. W. 2001, A&A, 367, 1000

Pols, O. R., Tout, C. A., Eggleton, P. P., & Han, Z. 1995, MNRAS, 274, 964

Sarazin, C. L. 1988, X-ray emission from clusters of galaxies, Cambridge Astrophysics Series, Cambridge: Cambridge University Press, 1988

Skinner, S., Nagase, F., Ozawa, H., & Itoh, M. 1996, Bulletin of the American Astronomical Society, 28, 1375

Skinner, S. L., Zhekov, S. A., Güdel, M., & Schmutz, W. 2002, ApJ, 579, 764

Skinner, S. L., Zhekov, S. A., Güdel, M., Schmutz, W., & Sokal, K. R. 2010, AJ, 139, 825

Smith, R. K., &Hughes, J. P. 2010, ApJ, 718, 583

Snowden, S.L., Egger, R., Freyberg, M.J., McCammon, D., Plucinsky, P.P., Sanders, W.T., Schmitt, J.H.M.M., Trümper, J., & Voges, W. 1997, ApJ485, 125

Snowden, S.L., Collier, M.R., & Kuntz, K.D. 2004, ApJ, 610, 1182

Snowden, S. L., Mushotzky, R. F., Kuntz, K. D., & Davis, D. S. 2008, A&A, 478, 615

Snowden, S. L., & Kuntz, K. D. 2011, Bulletin of the American Astronomical Society, 43, #344.17

Spitzer, L. 1962, Physics of Fully Ionized Gases, New York: Interscience (2nd edition), 1962

Steffen, M., Schönberner, D., & Warmuth, A. 2008, A&A, 489, 173

Stock, D. J., & Barlow, M. J. 2010, MNRAS, 409, 1429

Toalá, J. A., & Arthur, S. J. 2011, ApJ, 737, 100

Townsley, L. K., Feigelson, E. D., Montmerle, T., Broos, P. S., Chu, Y.-H., & Garmire, G. P. 2003, ApJ, 593, 874

van der Hucht, K. A., Cassinelli, J. P., & Williams, P. M. 1986, A&A, 168, 111

van der Hucht, K. A., Hidayat, B., Admiranto, A. G., Supelli, K. R., & Doom, C. 1988, A&A, 199, 217

Weaver, R., McCray, R., Castor, J., Shapiro, P., & Moore, R. 1977, ApJ, 218, 377

Wrigge, M., Wendker, H. J., & Wisotzki, L. 1994, A&A, 286, 219

Wrigge, M., Chu, Y.-H., Magnier, E. A., & Kamata, Y. 1998, IAU Colloq. 166: The Local Bubble and Beyond, 506, 425

Wrigge, M. 1999, A&A, 343, 599

Wrigge, M., & Wendker, H. J. 2002, A&A, 391, 287

Wrigge, M., Chu, Y.-H., Magnier, E. A., & Wendker, H. J. 2005, ApJ, 633, 248

Zhekov, S. A., & Park, S. 2011, ApJ, 728, 135

This 2-column preprint was prepared with the AAS LaTeX macros v5.2.